

Thermal transport in bent graphene nanoribbons

Jingchao Zhang and Xinwei Wang*

Cite this: *Nanoscale*, 2013, 5, 734

This work reports on a study of the phonon behavior and thermal transport in bent graphene nanoribbons (GNRs). Three peculiar phenomena are observed in bent GNRs during thermal transport. First, due to the high thermal conductivity of flexural mode (ZM) phonons in GNRs, energy separation is observed between the in-plane and out-of-plane phonon modes after a steady state heat flux is imposed on the system. Such energy separation can hold for about 50 nm from the heating region. Second, a thermal resistance is observed in the bending region of a 90° bent GNR system. This phenomenon is explained by the phonon energy scattering/reflection and the compressive strain in the bending structure. Different bending angles are investigated and it is proved that the bending resistance decreases with increasing bending angle. Finally, upon crossing the bending structure in GNRs, phonon packages preserve their vibrating mode instead of vibrating directions.

Received 22nd July 2012

Accepted 15th November 2012

DOI: 10.1039/c2nr31966g

www.rsc.org/nanoscale

1 Introduction

Graphene is a monatomic layer of carbon atoms that exhibits superior charge mobility and mechanical strength, as well as strong compatibility with existing planar silicon devices.^{1–5} Graphene nanoribbons (GNRs) occupy a rather special position in the study of micro/nanoscale materials, having a variety of striking properties that other carbon materials (such as diamond, carbon nanotubes or graphite) lack. Balandin *et al.*^{6,7} reported extremely high thermal conductivity (κ) values in the range of 4840 ± 440 to 5300 ± 480 W m⁻¹ K⁻¹ for mechanically exfoliated single layer graphene at room temperature (RT). Several groups have since measured the thermal conductivity of suspended graphene using different methods.^{8–11} Their measured κ values range from 1800 W m⁻¹ K⁻¹ to 5150 W m⁻¹ K⁻¹ near RT. While for supported monolayer graphene, much lower κ values have been measured at ~ 600 W m⁻¹ K⁻¹ at RT due to flexural phonon coupling with the substrate.^{10,12}

The experimental report on the thermal conductivity of graphene stimulated extensive numerical work on the subject. Using classical molecular dynamics (MD) simulation, Hu *et al.*¹³ calculated the thermal conductivity of a symmetric GNR with dimensions of 1.5×5.7 nm² to be around 2100 W m⁻¹ K⁻¹ at 400 K. Evans *et al.*¹⁴ reported a thermal conductivity at ~ 6000 W m⁻¹ K⁻¹ for a graphene sheet with dimensions of 10×10 nm² at 300 K. Other groups using equilibrium molecular dynamics (EMD)¹⁵ and nonequilibrium molecular dynamics (NEMD)¹⁶ came up with much lower thermal conductivities at 630 W m⁻¹ K⁻¹ and 218 W m⁻¹ K⁻¹ respectively for isolated graphene and armchair GNRs at 300 K. Recently, we argued that quantum

correction is of great importance in the numerical calculations of GNR's thermal conductivity.¹⁷ After applying quantum correction to MD temperature results, our calculated κ value for a 2.0 nm wide GNR with infinite length is 317 W m⁻¹ K⁻¹ at 300.6 K and 149 W m⁻¹ K⁻¹ at 692.3 K.

The exceptional thermal properties of graphene are partially due to its unique phonon transport mechanism in the 2-D system. The challenge of accounting for these phonon features gives the starting impetus to the study of graphene. There are three acoustic phonon branches, *i.e.* the in-plane longitudinal (LA) and transverse (TA) branches and the out-of-plane flexural (ZA) branch, which contribute to the thermal conductivity of graphene. Although for a long time it has been tacitly accepted that the in-plane acoustic phonons are dominant in the thermal transport of graphene,^{18–21} recent studies have proven that the fact is quite different. Saito *et al.*²² calculated the ballistic thermal conductance of graphene by investigating the dispersion relation of phonons and electrons. They proved that the ballistic phonon conductance of graphene below about 20 K is mainly determined by the out-of-plane acoustic mode (ZA branch) and the in-plane acoustic modes (LA and TA branches) cannot be ignored above 20 K. By measuring the thermal transport of single layer graphene (SLG) supported on amorphous SiO₂, Seol *et al.*^{12,23} performed a revised calculation and they showed that the ZA branch can contribute as much as 77% at 300 K and 86% at 100 K of the calculated thermal conductivity for suspended graphene due to the high specific heat and long mean scattering time of ZA phonons. Based on the exact numerical solution of the linear Boltzmann transport equation (BTE), Lindsay *et al.*^{24,25} calculated the lattice thermal conductivity (κ_L) of graphene at 300 K and it turned out that the dominant contribution to κ_L comes from the ZA branch, which is greater than the combined TA and LA contributions. A symmetry-based selection rule and the anomalously large

Department of Mechanical Engineering, Iowa State University, 2010 Black Engineering, Ames, IA 50011, USA. E-mail: xwang3@iastate.edu; Fax: +1-515-294-3261; Tel: +1-515-294-2085

density of states of flexural phonons are used to explain their results. Our previous study revealed the fact that in a GNR system, the ZA branch has peculiarly higher thermal conductivity than the LA and TA branches.¹⁷ Also, ZA↔ZA energy transfer is much faster than the ZA↔LA/TA phonon energy transfer. We have proved that under the influence of a moving or static localized heat source, the flexural mode (FM) phonons dissipate heat much faster than the longitudinal mode (LM) and transverse mode (TM) phonons, which gives rise to an energy inversion phenomenon at the system level.

Using a one-step mild chemical reduction and *in situ* self-assembly method, Chen and Yan²⁶ prepared 3D architecture of graphene under atmospheric pressure in an open system, which makes it possible to prepare 3D architecture of graphene on a large scale. Graphene has very high carrier mobility and a unique quantum spin Hall effect. These properties make graphene a promising material for electronic circuits and high-speed transistors.^{27,28} In these micro/nanoscale electronic devices, a single layer graphene has to fit the surface profile of its substrate. For the micro/nanostructured non-flat surface, the atomic bonding between graphene and the substrate will bend the graphene. Graphene is also an important material in many carbon-based polymer composites.^{29–31} The embedded graphene could help increase the thermal conductivity of the composites significantly. During sample preparation, various factors can cause the graphene to fold in the matrix material. Also, graphene is used in nanofluids to enhance the thermal conductivity.^{32–34} In the liquid environment, the single/multi-layer graphene will not be able to keep its 2D form and will be curved or folded within the liquid. However, in spite of existence of bent graphene in vast applications, little work has been done to reveal the thermal transport in 3D graphene structures, especially that in the bending region. In the present work, classic MD simulation based on the second generation of Brenner potential³⁵ is performed to investigate the thermal energy transport in bent and flat GNR systems. In the right-angle bent GNR system, three peculiar features about the phonon energy transport have been observed for the first time. The first one is energy separation among different phonon modes caused by the higher FM phonon thermal conductivity. The second one is phonon energy jump across the bending region, which is due to the phonon mode-conservation mechanism in the GNR system. Last but not least, an energy drop occurs when phonon packages pass through the bending region. Phonon scattering/reflection and localized compressive strain in the bending region help explain this local energy barrier. At the end, we discuss the influence of bending angle on thermal energy transport in bent GNR systems. Our results provide fundamental knowledge about graphene for thermal management applications in nanoelectronics.

2 Methodology and results

The second generation of Brenner potential:³⁵ reactive empirical bond-order (REBO), based on the Tersoff potential^{36,37} with interactions between C–C bonds is applied in our MD simulation. To prevent the free-standing GNR from curling and ensure

full structure relaxation during the thermal-equilibrium calculation, the GNR systems are bound within Lennard-Jones (LJ) walls in all directions that enclose all the atoms. In this work, the GNR systems have zigzag boundaries in the width direction and armchair boundaries in the length direction. The edge carbon atoms are not hydrogen-passivated. The walls interact with the GNR atoms *via* the 9/3 LJ potential $E_p = \epsilon[2/15(\sigma/r)^9 - (\sigma/r)^3]$, when $r < r_c$. r is the distance from the atom to the wall, and ϵ and σ are the LJ parameters, which are set to be 0.00284 eV and 3.4 Å respectively. Since the distance between adjacent carbon layers in graphite is 0.335 nm, we set this value as the initial distance between the LJ walls and the GNR boundaries.

2.1 Phonon energy transport in right-angle bent GNRs

To ensure effective heat transfer and stable performance of graphene in future microelectronics, interconnects and thermal management structure, thermal properties of bent graphene systems should be further studied. To the best of our knowledge, little research has been done on this subject. In this section, bent GNR systems of length 25.0 nm, 50.1 nm, 75.0 nm and 100.0 nm with a fixed width 2.0 nm are built. Each structure is warped at the middle plane in the length direction to form a right-angle structure. Construction of the GNR system is shown in the inset of Fig. 1(b). To keep the formation of the GNR system, LJ walls are applied in each direction of the system. Along its length direction the GNR is divided into sections each containing about 20 carbon atoms for the later temperature distribution study. The canonical ensemble (NVT) and micro-canonical ensemble (NVE) conditions are applied to the system in succession at temperature 50 K to equilibrate the system. A time step of 0.5 fs is used for all calculations. Hot and cold regions are then created in the simulation domain by adding kinetic energy ΔE_k in the hot region and removing the same amount from the cold one while preserving linear momentum at each time step. Four layers of carbon atoms at each end of the GNR system are chosen to add and subtract thermal energies respectively by scaling the velocity of each atom by the same factor χ . Given enough time, the system will reach the thermal equilibrium state again with a steady state heat flux flow (q'') in the length direction. Thermal energies of different phonon modes and the system are then post-processed to obtain the energy distribution along the length direction of the GNR system. Thermal energy (Q) added/subtracted equals 5.9×10^{-8} W for all structures. Since the layer distance in graphite is 0.335 nm, we use this value as the thickness for single layer graphene.^{6,7,10,14,17} The cross-sectional area (A_c) can then be calculated as 6.7×10^{-19} m². Therefore the heat flux in the length direction can be calculated from the equation $q'' = Q/A_c$, which equals 8.81×10^{10} W m⁻². To compare the energy evolution of different phonon modes and the whole system, a nominal temperature defined as $E_i/(1/2)k_B$ with unit K is used to represent the energy values in each direction and a value $E_T/(3/2)k_B$ with unit K stands for the system's total energy. Here E_i is the kinetic energy of carbon atoms in direction i ($i = x, y, \text{ or } z$), and E_T is the total kinetic energy of carbon atoms.

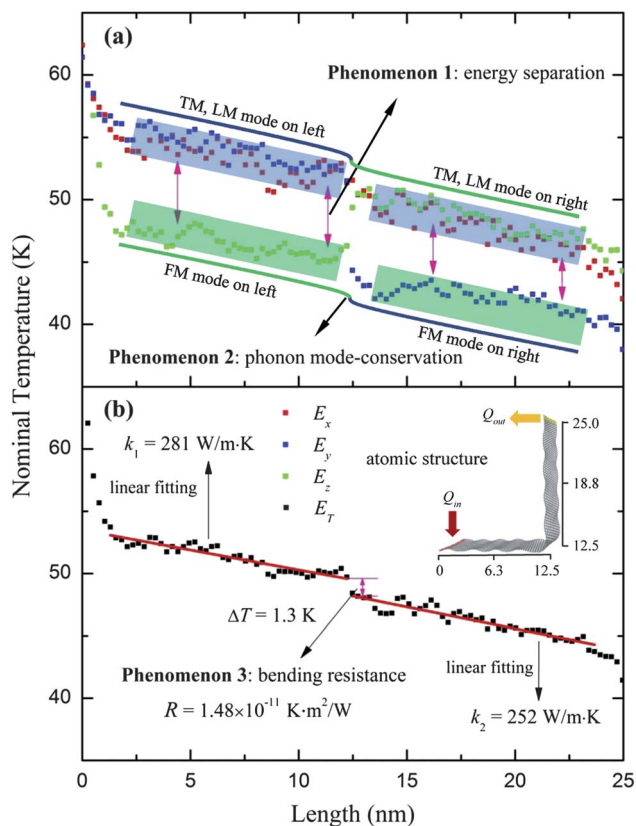


Fig. 1 Thermal transport in a $2.0 \times 25.0 \text{ nm}^2$ right-angle bent GNR system. The E_y and E_z exchange their values upon crossing the bending structure, indicating phonon mode-conservation in GNR systems. Bending resistance is observed around the bending area. Thermal conductivities of two flat GNR regions are calculated by linear fitting. The calculated κ and R values denoted in (b) are before quantum corrections.

The nominal temperature results of the $2.0 \times 25.0 \text{ nm}^2$ right-angle bent GNR are shown in Fig. 1(a) and (b). Since the GNR is warped at the middle plane, the bending structure is located at 12.5 nm position in the length direction. The black, red, blue and green data points are for the kinetic energy of the system (E_T), x , y , and z direction components: E_x , E_y , and E_z , respectively. Three crucial phenomena are observed in these two figures. The first one is the phonon energy separation among different phonon modes, which happens all the way along the length direction. The second one is that upon the phonon energies crossing the bending structure, an energy jump between E_y and E_z is observed. After the phonon energies go across the bending region at 12.5 nm, E_y and E_z exchange their positions and E_y becomes the lowest energy value in the system. Consequently, the phonon energy will flow from E_x and E_z to E_y after they pass through the right-angle region until they reach the same level. Based on this result, we conclude that when the phonons pass through a bending area, the phonon modes are preserved, *i.e.* the flexural phonon branch remains vibrating in the out-of-plane direction after it passes through the bending structure and the in-plane TM and LM branches keep vibrating perpendicular and along the phonon propagating direction. Detailed proof is given in later sections using separated phonon mode excitation. Phenomena 1 and 2 are denoted in Fig. 1(a).

Last but not least, the third phenomenon, an energy drop across the bending area, is observed for each energy mode, indicating that an energy barrier exists in the bending region which causes a local thermal resistance (R) between the horizontal and vertical parts of the GNR system. R can be calculated as $R = \Delta T/q''$, where ΔT is the temperature drop (K) and q'' the heat flux along the path of heat flow (W m^{-2}). ΔT is evaluated at 1.3 K in the $2.0 \times 25.0 \text{ nm}^2$ GNR system and the corresponding bending resistance is $1.48 \times 10^{-11} \text{ K m}^2 \text{ W}^{-1}$ before quantum correction. Phenomenon 3 is shown in Fig. 1(b). The thermal conductivity values of the horizontal and vertical parts of the GNR are calculated using Fourier's Law: $q'' = -\kappa \nabla T$, where ∇T is the temperature gradient. It is worth noting that in general both electrons and phonons contribute to the thermal transport in graphene. In this work the MD temperatures for all GNR systems are around 50 K, which correspond to $\sim 300 \text{ K}$ after quantum correction. And at this temperature, the phonon's contribution to graphene's thermal conductivity is nearly 100 times greater than that of electrons.²² Besides, according to the Wiedemann–Franz law, the estimated contribution of electrons to graphene's thermal conductivity is less than 1% at room temperature.⁸ This is also consistent with the observation for the thermal conductivity of individual carbon nanotubes (CNTs).^{38,39} From these prospects, previous MD simulation studies about the edge and length effect on graphene's thermal conductivity also just consider the phonon's contribution and electron's contribution is neglected.^{13,14,16,40,41} Therefore, in this work we only consider the phonon's contribution to GNR's thermal conductivity. By linear fitting the data from these two parts, the κ values are calculated to be $281 \text{ W m}^{-1} \text{ K}^{-1}$ and $252 \text{ W m}^{-1} \text{ K}^{-1}$ for the horizontal and vertical parts before quantum correction. It is observed that the thermal conductivities for the horizontal and vertical parts are different, which is mainly caused by two reasons. First, since the horizontal part has the heat source and vertical part has the heat sink, the phonon energy distributions are different in these two parts, as is shown in Fig. 1(a). Also, the total temperatures for these two parts are different, and the thermal conductivity of graphene is temperature dependent. Second, the calculation uncertainty also contributes to the differences. In the linear fitting process, we have to manually choose the fitting region to calculate the thermal conductivities and the results will be slightly different even if we change the fitting range by several points. We tried our best to choose the most reasonable fitting region, yet the calculation uncertainty is inevitable. Thus, we think the 10% thermal conductivity difference for these two parts is acceptable. Nominal temperature results for right-angle GNRs of length 50.1 nm, 75.0 nm and 100.0 nm are shown in Fig. 2. The temperature drop in the bending structure of each system is 1.7 K, 1.7 K, and 4.3 K respectively and the corresponding thermal resistances are 1.93×10^{-11} , 1.93×10^{-11} , and $4.88 \times 10^{-11} \text{ K m}^2 \text{ W}^{-1}$ before quantum correction. The thermal resistance is also calculated for the 200.0 nm right-angle GNR and the result is $4.2 \times 10^{-11} \text{ K m}^2 \text{ W}^{-1}$. Both energy separation and energy drop phenomena are observed in all cases.

In MD simulations, the temperature can be readily calculated from the time average kinetic energy of atoms in the

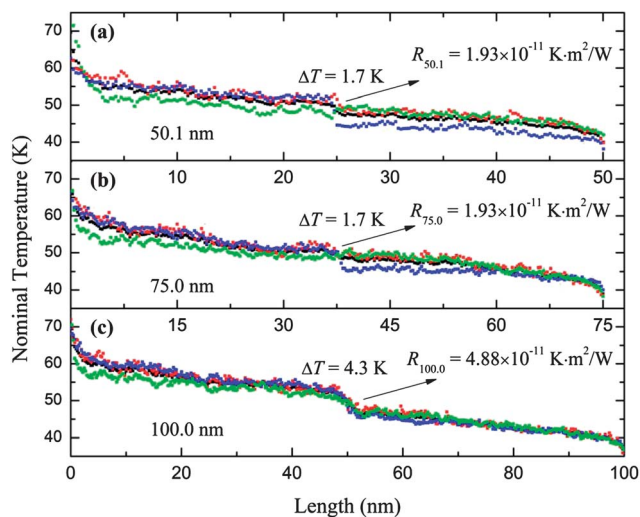


Fig. 2 Nominal temperature distributions in different length 50.1 nm, 75.0 nm and 100.0 nm right-angle GNR systems. Each GNR structure has a fixed width of 2.0 nm. The bending resistance values denoted in the figures are without quantum corrections.

sample section within the simulation time using the energy equipartition theorem:

$$\langle E_k \rangle = \sum_1^N \frac{1}{2} m v_i^2 = \frac{3}{2} N k_B T_{MD}, \quad (1)$$

where $\langle E_k \rangle$ is the mean kinetic energy, v_i the velocity of atoms, m the atomic mass, N the number of atoms in the system and k_B the Boltzmann constant. However, it is worth noting that this method is valid only at high temperatures ($T \gg T_D$, T_D is the Debye temperature). When the system temperature is lower than the Debye temperature, it is necessary to apply quantum correction to the MD temperature.^{13,42,43} Since the Debye temperature of graphene is around 2300 K,⁴⁴ while in our calculations, the MD temperature for the GNR system is around 50 K. The huge difference between them makes it a must in this work to apply quantum corrections to the MD temperatures. In our previous work,¹⁷ we derived the quantum correction equation for a two-dimensional GNR model as

$$T_{MD} = \frac{2}{3} T_{LA} x_{LA}^{-3} \int_0^{x_{LA}} \frac{x^2}{e^x - 1} dx + \frac{2}{3} T_{TA} x_{TA}^{-3} \int_0^{x_{TA}} \frac{x^2}{e^x - 1} dx + \frac{1}{3} T_{ZA} x_{ZA}^{-2} \int_0^{x_{ZA}} \frac{x}{e^x - 1} dx, \quad (2)$$

where T_{MD} is the temperature in MD simulation, T_{LA} , T_{TA} , and T_{ZA} are the Debye temperatures of three different acoustic modes in GNRs, which are 2840 K, 1775 K, and 1120 K respectively. x_{LA} , x_{TA} , and x_{ZA} are the ratios of corrected temperatures (temperatures after quantum correction, denoted as T) and Debye temperatures. Given the values of T_{MD} , which are generated in the MD simulation process, x_{LA} , x_{TA} and x_{ZA} values can be determined by the inverse form of eqn (2). In our work, first of all, a wide range of T values are used in eqn (2) to get x_{LA} , x_{TA} , and x_{ZA} , and calculate the corresponding T_{MD} . After we

obtain the relations (a curve) between T_{MD} and T , the corrected temperatures can be calculated by interpolation based on a specified T_{MD} . One good way to check the validity of our quantum correction method is the calculation of graphene's specific heat. When the MD temperature of the GNR system is around 300 K, the specific heat value before quantum correction is calculated to be $2.021 \times 10^3 \text{ J kg}^{-1} \text{ K}^{-1}$. However, after quantum correction, the specific heat reduces to $1.528 \times 10^3 \text{ J kg}^{-1} \text{ K}^{-1}$ and the temperature after quantum correction is around 692.3 K. This specific heat value is very close to that of graphite $1.519 \times 10^3 \text{ J kg}^{-1} \text{ K}^{-1}$ at 700 K.⁴⁵ After applying quantum correction to previous results of thermal conductivity and bending resistance, we get the revised κ values as $109 \text{ W m}^{-1} \text{ K}^{-1}$ and $92.7 \text{ W m}^{-1} \text{ K}^{-1}$ for the horizontal and vertical parts and revised R values as $3.93 \times 10^{-11} \text{ K m}^2 \text{ W}^{-1}$ for the $2.0 \times 25.0 \text{ nm}^2$ GNR. The thermal conductivity results are higher than our previous calculated κ values,¹⁷ which could be caused by the difference between dynamic and steady state thermal transport processes involved in the thermal conductivity definition. For low-dimensional systems such as GNRs, the definition of cross-sectional area has certain arbitrariness. In previous experimental studies of graphene's thermal conductivity, Balandin *et al.*^{6,7} used the value of $0.35 \pm 0.01 \text{ nm}$ as the thickness of single layer graphene. Lee *et al.*⁹ and Cai *et al.*¹⁰ used the SLG thickness of 0.335 nm in their calculations. Most of the numerical work studying the thermal conductivity of graphene chose the value of 0.335 nm as the thickness,^{13,14,17,41,46} yet only the study by Guo *et al.*¹⁶ used the value of 0.144 nm in graphene's thermal conductivity calculations. Therefore, our calculations of GNR's thermal conductivity uses the same thickness value (0.335 nm) as used in most of the experimental and numerical work. This provides a common base when comparing our results with those by other researchers. As for the 50.1 nm, 75.0 nm and 100.0 nm length GNRs, the corrected bending resistance values are $5.04 \times 10^{-11} \text{ K m}^2 \text{ W}^{-1}$, $5.04 \times 10^{-11} \text{ K m}^2 \text{ W}^{-1}$, and $1.29 \times 10^{-10} \text{ K m}^2 \text{ W}^{-1}$ respectively. Yue *et al.*⁴⁷ calculated the interfacial thermal resistance between the graphene layer and the 4H-SiC substrate to be 7.01×10^{-10} and $8.47 \times 10^{-10} \text{ K m}^2 \text{ W}^{-1}$ for surface heat fluxes of 3.0×10^9 and $1.0 \times 10^{10} \text{ W m}^{-2}$ respectively. Other groups using the 3ω method measured the contact resistance between graphene and silicon dioxide in the range of 5.6×10^{-9} to $1.2 \times 10^{-8} \text{ K m}^2 \text{ W}^{-1}$.⁴⁸ It could be seen that our calculated R values are much lower than the interfacial thermal resistance between the graphene layer and other materials, which is as expected since there is no flexural phonon coupling and scattering at those interfaces.^{20,21}

2.2 Energy separation in flat GNRs

To further explore the phonon energy separation observed in bent GNR systems, different lengths (25.0, 50.1, 75.0 and 100.0 nm) of flat GNRs with a fixed width of 2.0 nm are built and studied. Schematic construction of a flat GNR is shown in Fig. 3. Following the same routines used in the bent GNR systems, the NVT and NVE conditions are applied to equilibrate each structure at 50 K and a time step of 0.5 fs is used for all calculations.

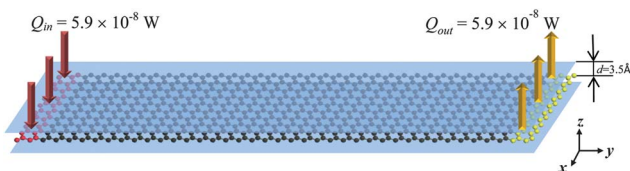


Fig. 3 Atomic structure of the flat GNR system studied for energy separation. The Lennard-Jones (LJ) potential walls are applied in all dimensions. To make a clear schematic description, only the top and bottom LJ walls are shown. Distance between each LJ wall and the GNR plane is set as 3.5 Å initially. A thermal energy of 5.9×10^{-8} W is added/subtracted from the red and yellow areas respectively.

Hot and cold regions are then created to induce a steady state heat flux flow (q'') in the length direction and nominal temperature data are extracted and averaged for each unit cell.

Take the 2.0×25.0 nm² flat GNR as an example, after 200 ps NVT and 50 ps NVE thermal equilibrium calculations, the system reaches the steady state at 50 K. Heat flux is applied to the system for 100 ps. After the system reaches the steady state, energy data are collected and averaged for the next 50 ps. The nominal temperature distribution of the system and its decomposition are shown in Fig. 4(a). It is seen from this figure that E_x and E_y values are almost the same along the length direction. However, E_z values are much lower than them. The energy differences are decreasing from the heating to cooling region, indicating energy transfer from E_x and E_y to E_z along the flat GNR until the three energy components reach the same level. To verify our speculation, nominal temperature distributions of 50.1 nm, 75.0 nm and 100.0 nm length GNRs are calculated and the results are shown in Fig. 4(b)–(d). Energy separation is observed in all cases and the three energy components reach the same level at around 50 nm.

For this first-time observed phonon energy behavior in graphene, our understanding of the driving force behind it is the much higher thermal transport capability by the flexural mode phonons. The mechanism of the phonon energy transfer is presented in Fig. 4(e). In the hot region, local phonon energies of the GNR will increase dramatically when the heat flux is added to the area. This high local energy will then be transmitted to the low nominal temperature regions by E_x , E_y and E_z . As mentioned above, despite the fact that the ZA phonons have vanishing group velocities for wave vector $q \rightarrow 0$, its high specific heat and long phonon mean scattering time make the ZA branch dominant in graphene's thermal conductivity. The large density of states and phonon scattering selection rule for the ZA branch also contribute to its anomalously large thermal conductivity.^{12,24} Therefore, the local flexural mode phonons in the hot region will transfer heat much faster than the in-plane modes phonons, giving rise to the lower E_z values along the length direction in which heat is conducted. Consequently thermal energies keep transferring from the in-plane phonons to the flexural phonons until they reach the same level.

2.3 Phonon mode-conservation

In general, the thermal conductivity of a solid arises from two distinct contributions: one from phonons and the other one from electrons. In this work, only lattice thermal conductivity is

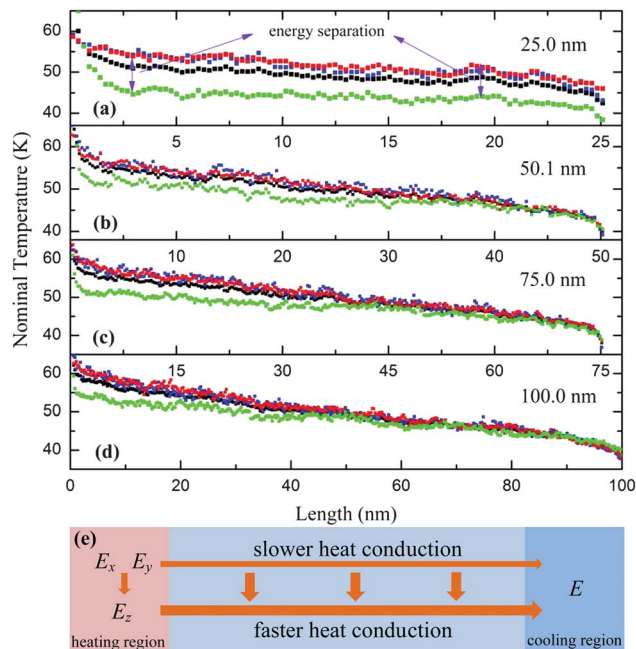


Fig. 4 Nominal temperature distributions in flat GNR systems of different lengths (a) 25.0 nm, (b) 50.1 nm, (c) 75.0 nm and (d) 100.0 nm. Each GNR structure has a fixed width of 2.0 nm. A thermal energy of the same value 5.9×10^{-8} W is added/subtracted in the selected regions for all systems. It is observed that energy separation happens at short distances in the heat flux flow direction and disappears at around 50 nm. (e) A schematic explanation of the thermal transport mechanism in short GNRs. The ZM branch has higher thermal transport ability than the in-plane TM and LM branches. Therefore E_z is lower than E_x and E_y and the latter will keep transferring energies to E_z until they reach the same level.

considered. Consequently, phonon package propagations determine the thermal transport properties in the GNR system. To explain the bending resistance in the right-angle bent GNR system, it requires further investigation of phonon transport in the bending region. For this purpose, a 2.0×50.1 nm² right-angle GNR system is built. Construction of the GNR is the same as shown in the inset of Fig. 1(b). The system is equilibrated at 50 K after 300 ps NVT and 50 ps NVE calculations. Then four layers of carbon atoms at one end of the GNR system are grouped to apply a stretching force (F), which is added to each atom in the group and has a value of 1.0 eV Å⁻¹. The time step is 0.5 fs in the thermal equilibrium calculations and 0.05 fs for the stretching. A short period of time 25 fs is used for the stretching process (phonon excitation). By applying the stretching force in the x , y and z directions separately, TM, LM and ZM phonon packages are generated separately in the GNR system, which propagate from the excitation area to the other end along the length direction.

Spatio-temporal energy contours are plotted in Fig. 5 for the LM and ZM phonon packages. Fig. 5(a) and (b) show energy contours of E_y and E_z after LM phonon excitation (E_y) at the left end. Fig. 5(c) and (d) show energy contours of E_z and E_y results after ZM phonon excitation (E_z) at the left end. The bending position (25.0 nm) for each structure is denoted by the dashed lines. In Fig. 5(a), after the excitation, a phonon package wave (E_y) is generated propagating along the length direction until it

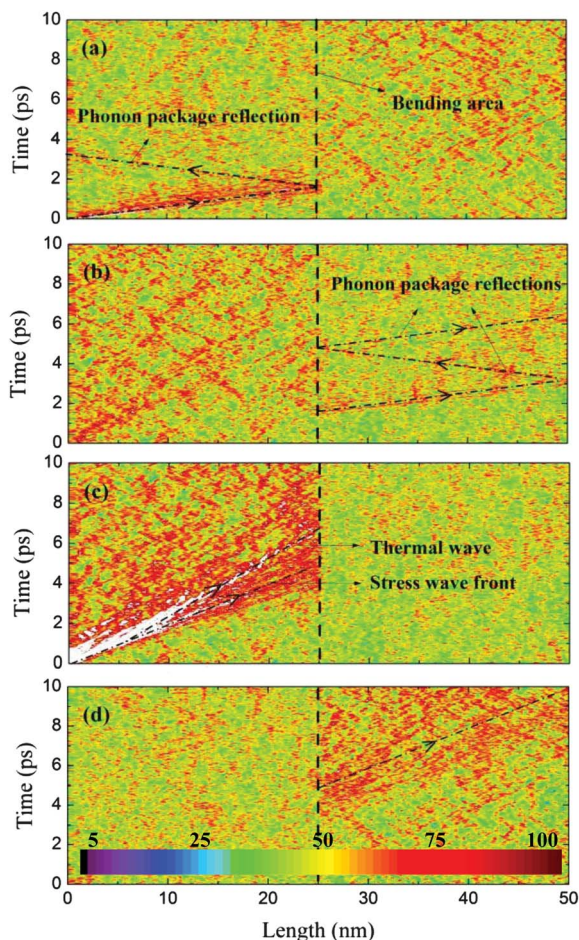


Fig. 5 Spatio-temporal iso-energy contours for the right-angle GNR structure. (a) and (b) represent E_y and E_z evolution after the LM phonon excitation (E_y) at the left end. (c) and (d) are for E_z and E_y evolution after the ZM phonon excitation (E_z) at the left end. Phonon mode-conservation is observed for the LM and ZM phonon branches. Phonon package reflections are also observed in the middle-plane at the bending region.

confronts the bending plane. A reflection wave has been observed in the corner. The disappearing LM phonon package wave in Fig. 5(a) emerges in the right part of Fig. 5(b) and these two waves are continuous since they share the same starting/ending point and have the same slope. This proves the fact that after the LM phonons pass through the bending area, their vibrating path changes from the y direction (E_y) on the left side to the z direction (E_z) on the right side. The phonon mode is preserved instead of the absolute vibrating direction. Reflection waves are also found in the bending plane in Fig. 5(b). Despite the fact that the phonon package waves in Fig. 5(a) and (b) are continuous, the phonon package energies are dramatically reduced upon crossing the bending corner since the wave fronts in Fig. 5(b) are much weaker and thinner than those in Fig. 5(a). A similar phenomenon is observed for the ZM phonon excitation case in Fig. 5(c) and (d). After the excitation is applied in the z direction, ZM phonon package waves are generated in the left part of Fig. 5(c) and propagate to the right of the system. As mentioned above, since the ZM branch is dominant in GNR's thermal conductivity, the ZM phonon packages in Fig. 5(c) and

(d) are much stronger than the LM phonon packages. This confirms the point that energy separation in GNRs is caused by the strong thermal transport capability of the ZM branch.

From the above discussions, we can safely draw a conclusion that after the phonon packages pass through the bending structure of GNRs, instead of remaining in their absolute vibrating directions, they preserve their vibrating modes. To sum up, the spatio-temporal iso-energy contours indicate that the flexural phonons will always vibrate in the out-of-plane direction of the GNR while the longitudinal phonons will always vibrate along the thermal conduction direction. Also, phonon scattering and reflections are observed in the bent structure.

Apart from the phonon packages propagation and reflection phenomena mentioned above, phonon coupling between in-plane and out-of-plane phonons is also observed. It could also be seen that E_z values in the left part of Fig. 5(b) become higher than E_y in the left part of Fig. 5(a) as the LM phonon package propagates. E_z in the left part of Fig. 5(c) remains higher than E_y in the left part of Fig. 5(d). This confirms our previous research results that the in-plane TM and LM phonons have a higher energy transfer rate than the out-of-plane ZM phonons and the latter are inclined to transport thermal energies to themselves rather than to other phonon modes. In the left part of Fig. 5(c), we can clearly see that a thermal wave is generated in the length direction as the ZM package propagates. When the thermal-relaxation time of the phonons is large, the thermal-wave effect will be more prominent. Therefore, the ZM mode is more significant than the TM and LM modes with respect to GNR's thermal conductivity. From Fig. 5(a) and (c), the group velocities for the LM and ZM phonons are calculated to be 15.34 km s^{-1} and 5.05 km s^{-1} respectively. A theoretical study of the second sound wave under the linear approximation for three-dimensional materials shows that the thermal wave propagation velocity is $c = v_g/\sqrt{3}$,⁴⁹ where v_g is the group velocity. For a two-dimensional GNR, this relation should be modified as $c = v_g/\sqrt{2}$.⁵⁰ In Fig. 5(c), the thermal wave propagation velocity is calculated to be 3.43 km s^{-1} for the ZM mode, as denoted by the dashed line. Based on the group velocity in Fig. 5(c), the thermal wave speed is predicted to be $c = v_g/\sqrt{2} = 5.05/\sqrt{2} = 3.57 \text{ km s}^{-1}$. This value agrees well with the thermal wave speed 3.43 km s^{-1} observed in Fig. 5(c).

2.4 Energy barrier across the bending region

Two distinct types of parameters control the effective thermal conductivity of GNRs: thermodynamic parameters such as temperature and pressure/strain, and extrinsic parameters such as impurities, defects and bounding surfaces. In this work, all GNR models are pristine without the influence of the latter parameters, thus only temperature and strain-stress effects should be considered. An energy barrier is observed in the bending structure of the right-angle GNR and it is necessary to investigate if there is a local strain in this area. To take a closer look at the structure deformation caused by the bending, the radial distribution function (RDF) is used to explore the atomic structure change in the bending area. The RDF results for both flat and bending regions are shown in Fig. 6. It is seen that the

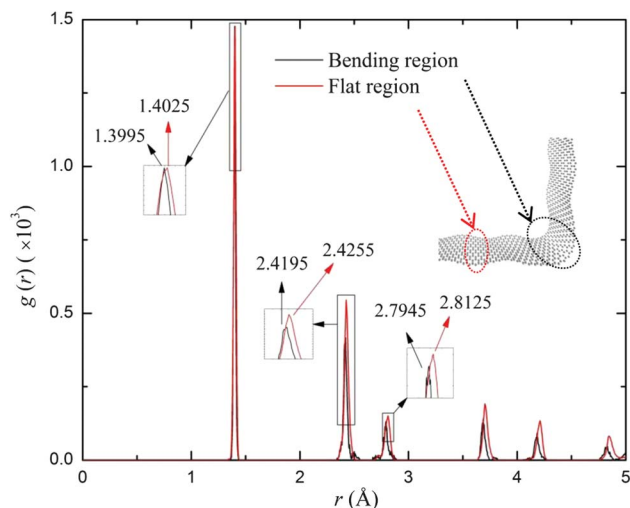


Fig. 6 Radial distribution function (RDF) of the flat and bending areas in the $2.0 \times 50.1 \text{ nm}^2$ right-angle bent GNR system. The black and red lines represent the RDF at the bending area and the flat area. The RDF for the bending area shows a smaller atomic distance than that in the flat area, indicating a compressive strain in the bending structure.

nearest neighboring distance in the bending area of GNRs is shorter than that in the flat area, indicating that a local compressive strain is generated in this area. By comparing the positions of the first peaks in Fig. 6, the compressive strain (ϵ) in the bending area is calculated to be -2.14×10^{-3} . Given the nearest neighboring distance in an exact hexagonal structure, the second and third nearest neighboring distances could be calculated accurately. In Fig. 6, the nearest neighboring distance in the bending region is 1.3995 \AA , which corresponds to the theoretical second and third nearest neighboring distances of 2.424 \AA and 2.799 \AA respectively. In the RDF results, the second and third nearest neighboring distances in the bending region are 2.4195 \AA and 2.7945 \AA , respectively. The slight differences between the theoretical and calculated values indicate that the hexagonal structure still holds good in the bending area. Unlike bulk materials such as silicon and diamond whose thermal conductivity will increase due to a compressive strain in the system, the single layer nature of GNRs makes it have a decreased thermal conductivity under either compressive or stretch strains.^{51,52} Because when a compressive strain is applied to the GNR structure, buckling in the out-of-plane direction will occur, resulting in an increasing phonon scattering rate and thus a reduced thermal conductivity. Therefore, it is conclusive that a free-standing GNR system will have a higher thermal conductivity than those with stains. In our case, since there is a compressive strain in the bending area of the GNR, the local thermal conductivity will drop, which constitutes one of the reasons for the bending resistance in this region.

The RDF for the 25.0 nm , 75.0 nm and 100.0 nm bent GNRs is also calculated. It is worth noting that the local stain in the bent structures cannot only be calculated from the position of the first peaks, the second and third peak differences can also be used to evaluate the local strain. By comparing the first peak

positions, the local strain values are calculated to be 0 , -2.14×10^{-3} , 0 and -6.77×10^{-3} respectively for the 25.0 nm , 50.1 nm , 75.0 nm and 100.0 nm right-angle bent GNRs. From the second peak positions, the strains are calculated to be -4.74×10^{-3} , -2.47×10^{-3} , -1.44×10^{-3} and -6.18×10^{-3} respectively. At last, the third peak positions give strain results of -4.27×10^{-3} , -6.4×10^{-3} , -9.6×10^{-3} and -6.22×10^{-3} respectively. The zero strain based on the first-peak position means that the nearest atomic distance is not altered in the bending area. Instead, the structure is twisted, and the extent of twisting is reflected by the strains calculated from the second and third RDF peaks. From the above results, it is clear that the local strain of the 100.0 nm case is much larger than the others with respect to the first and second peaks. This much larger strain will give much stronger phonon scattering than other cases, and lead to a larger thermal resistance. According to Li *et al.*,⁵¹ the thermal conductivity of graphene decreases with increasing local strain and the phonon scattering becomes stronger as the local strain increases. Therefore, the thermal resistance in the bending structure will also increase with the local strain. This explains the highest thermal resistance for the 100.0 nm bent GNR shown in Fig. 2(c) in our four calculated cases.

In the end, the bending resistance in the right-angle bent GNR is mainly caused by two factors: one is the phonon wave package scattering and reflections at the bending area; and the other one is the compressive strain in the bending structure which increases the phonon scattering and causes a thermal conductivity decrease.

3 Discussion

To further investigate the effect of bending angles on the thermal transport in GNRs, a 135° bent GNR system with dimensions of $2.0 \times 50.1 \text{ nm}^2$ is built. After thermal equilibrium calculations at 50 K , thermal energy of $5.9 \times 10^{-8} \text{ W}$ is added/subtracted at each end of the system separately and the nominal temperature distribution results are shown in Fig. 7. The atomic structure is shown in the inset of Fig. 7. No obvious bending resistance or thermal conductivity changes are observed in this figure, yet energy separation still exists until the phonon energies reach the same level at $\sim 50 \text{ nm}$ position, similar to the flat GNR cases shown in Fig. 4. From above cases, it can be summarized that the energy barrier decreases with increasing bending angle. Actually, we also consider including the bent graphene structures for the range of 0° to 90° . For example, we tried to build a 45° bent GNR structure to compare with previous cases but at the beginning stage of our calculations, we found that the initial distance between the carbon atoms around the bending corner is too close that they bounced away instantly when the thermal equilibration starts. We try to solve this problem by reducing the time step from 0.5 fs to 0.05 fs and adjusting the LJ potential wall distance, but still the bent structure could not hold. Therefore we did not report 0° to 90° bending cases in this work and our conclusions just apply to 90° to 180° bent GNRs. In our future work, efforts will be taken to obtain 0° to 90° bent GNR structures by increasing either the

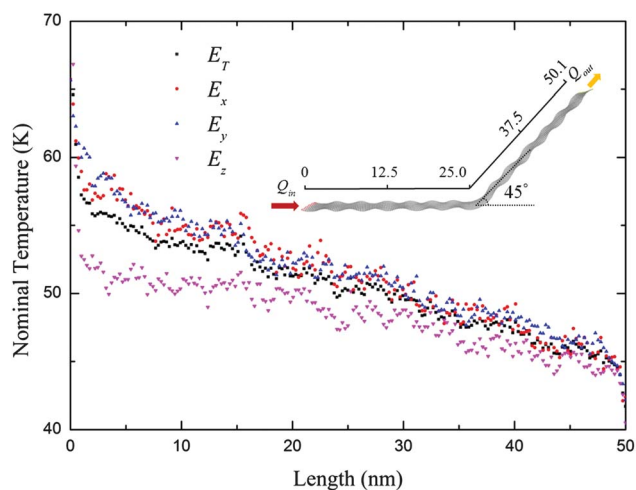


Fig. 7 Nominal temperature distributions for the 135° bent GNR with dimensions of $2.0 \times 50.1 \text{ nm}^2$. Atomic structure of the system is shown in the inset. Energy separation is observed in this structure, yet no obvious bending resistance or energy jump has been found.

GNR length or the strength of the GNR-wall interaction potential.

In the end, we discuss the 9-3 LJ potential walls' effect on the thermal transport in GNRs. It is true that the LJ potential walls will affect the out-of-plane form of the GNR and also the radius of curvature in the bending structure, which makes above reported thermal conductivity and thermal resistance results dependent on the 9-3 LJ potential parameters chosen in this work. Intuitively, the strength of the LJ potential controls the degree of bending for a GNR and its effective curvature in the bent region. The stronger the potential is, the larger the curvature and thermal resistance will be. This logic is supported by the results calculated above for different GNR lengths. A decrease in the GNR length would decrease the torque from GNR-wall interaction forces that counterbalance the internal straightening forces in the GNR due to bent deformations and, thus, should decrease the radius of curvature and the thermal resistance of the bent region. Since the bent GNRs are enclosed by potential walls in all directions, the bending position is fixed for a specific GNR system, which also contributes to the variation of thermal resistance values since the bending position will also affect the R results for bent GNRs. The LJ parameters used in this work are balanced results that are able to keep the formation of the bent GNR while ensuring that the system is not over-suppressed by the LJ walls. In other words, the LJ potential we applied is not an extreme case but properly adjusted. This could be seen from the fact that the atomic configurations for the obtuse angle (90° – 180°) bent GNRs are well maintained while the LJ potential is not so strong to be able to hold an acute angle (0° – 90°) bent structure. To study the thermal properties of a bent GNR, it is necessary to apply the L-J walls to the system. Otherwise the system will have spurious global rotation in the simulation. The LJ potential walls are intrinsically different from a substrate used in a supported graphene.⁵³ The 9-3 LJ potential is commonly used to model the interaction between

atoms with a flat structureless solid wall or *vice versa*. This soft repulsive potential wall will generate a force on the atoms in the direction perpendicular to the wall. The van der Waals force between the GNR and the LJ wall is much weaker than the covalent bond force between the carbon atoms in graphene. Since the potential walls are fixed in position (motionless), no external work will be done to the walls or to the GNR system, *i.e.*, there is no energy exchange between the GNR and the LJ walls. And this is the most important difference between the LJ wall and a substrate. The thermal conductivity of a supported graphene will decrease due to the out-of-plane (ZA) phonon scattering and energy coupling with the substrate. However, when the graphene is sandwiched between structureless LJ potentials, the phonons will have specular reflections on the walls. This specular reflection of phonons will not affect the thermal conductivity and thermal resistance of graphene. Nevertheless, the application of the LJ walls will affect the phonon dispersion relations of graphene and different choices of ϵ and σ could lead to different phonon energy distributions in the sandwiched GNRs. Under such scenario, the existence of potential walls will affect the calculated thermal conductivities and thermal resistances. From above discussions, it is conclusive that the LJ walls used in this work affect the calculated thermal properties of bent GNRs to a very limited extent.

Extra calculations have been done to elaborate on the above explanations. The ϵ and σ values of the 9-3 LJ potential are reduced to half ($\epsilon = 0.00142 \text{ eV}$, $\sigma = 0.17 \text{ nm}$) separately to compare the thermal resistance (R) and thermal conductivity (κ_h and κ_v) change with previous cases (right-angle bent). The comparison results are shown in Fig. 8. First, it is observed that the parameter σ plays a more important role than ϵ in the thermal resistance of bent GNRs. For example, when σ is reduced to half, thermal resistances of the 25.0, 50.1 and 75.0 cases are suppressed to zero, yet when ϵ is reduced to half, the

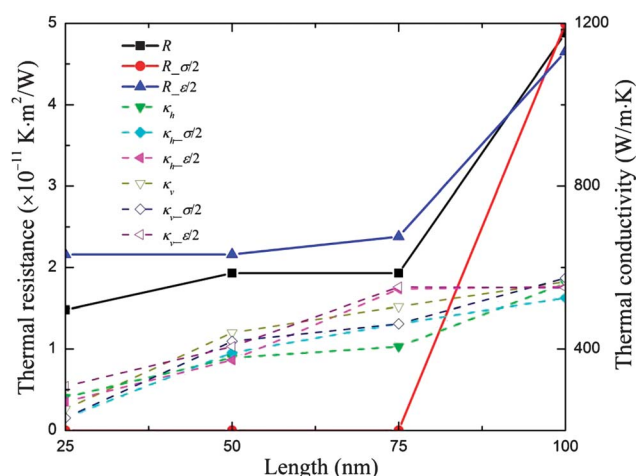


Fig. 8 Thermal resistance and thermal conductivity comparison with ϵ and σ reduced to half separately. It is observed that when σ is reduced to half, the R values are suppressed to zero for the 25.0 nm, 50.1 nm and 75.0 nm cases. While when ϵ is reduced to half, the R values just change slightly. The thermal conductivities vary in a small range when different ϵ or σ are used and increase with the GNR length. All the results are without quantum corrections.

R values remain almost the same. It is known that in the 9-3 LJ potential $E_p = \varepsilon[2/15(\sigma/r)^9 - (\sigma/r)^3]$, ε stands for the depth of the weakly attractive well and σ represents the separation distance at which the LJ potential changes sign. When σ is reduced to half, the first and second parts in the bracket are reduced to 0.002 and 0.125 times their original values separately. While when ε is reduced to half, the E_p value just changes by 50%. Therefore, it is clear that the strength of the LJ potential is more sensitive to σ . Thermal conductivities of the horizontal (κ_h) and vertical (κ_v) parts of the bent GNRs are also calculated with different ε and σ values. It is found that the thermal conductivities do not change much with either ε or σ reduced to half. Take the $2.0 \times 100.0 \text{ nm}^2$ GNR as an example, by only reducing σ to 0.17 nm, the thermal conductivity for the horizontal part of the 100.0 nm bent GNR changes from $561 \text{ W m}^{-1} \text{ K}^{-1}$ to $525 \text{ W m}^{-1} \text{ K}^{-1}$ while the thermal conductivity for the vertical part changes from $565 \text{ W m}^{-1} \text{ K}^{-1}$ to $574 \text{ W m}^{-1} \text{ K}^{-1}$. The thermal resistance in the bent region changes from $4.88 \times 10^{-11} \text{ K m}^2 \text{ W}^{-1}$ to $4.99 \times 10^{-11} \text{ K m}^2 \text{ W}^{-1}$. By only reducing ε to 0.00142 eV, the thermal conductivity becomes $553 \text{ W m}^{-1} \text{ K}^{-1}$ and $550 \text{ W m}^{-1} \text{ K}^{-1}$ for the horizontal and vertical parts, and the thermal resistance in the bent region is $4.65 \times 10^{-11} \text{ K m}^2 \text{ W}^{-1}$. The κ_h and κ_v values with half ε or σ values are shown in Fig. 8. The thermal resistance and thermal conductivity values are without quantum corrections. Therefore, it is conclusive that the change of 9-3 LJ potential parameters does not make a substantial effect on the phonon thermal transport in bent GNRs, unless a very strong wall potential and a very narrow wall–GNR distance is used. The LJ potential wall's effect on the thermal conductivity of flat GNRs is also investigated systematically. The 25.0 nm and 50.1 nm flat GNRs are used to calculate the phonon energy distributions with $\varepsilon = 0.00142 \text{ eV}$ and $\sigma = 0.17 \text{ nm}$. Compared with previous cases, the thermal conductivity of the 25.0 nm flat GNR changes from $355 \text{ W m}^{-1} \text{ K}^{-1}$ to $325 \text{ W m}^{-1} \text{ K}^{-1}$ after the ε and σ are reduced by 50%. As for the 50.1 nm flat GNR, the thermal conductivity just changes very little: from $399 \text{ W m}^{-1} \text{ K}^{-1}$ to $393 \text{ W m}^{-1} \text{ K}^{-1}$. From the above comparisons, it is concluded that the 9-3 LJ potential walls applied in this work do not have substantial effect on the thermal transport in bent or flat GNRs.

4 Conclusion

In this work, phonon thermal transport in bent GNR systems was studied systematically and three new phenomena were observed. In the 3D right-angle bent GNR systems, energy separation emerged between the in-plane and out-of-plane phonon modes. To further exploit the energy separation phenomenon, flat GNR systems of different lengths: 25.0 nm, 50.1 nm, 75.0 nm and 100.0 nm with a fixed width 2.0 nm were built, and energy separations were observed in all structures after a steady state heat flux flow was added. Strong thermal transport capability of the ZM phonons was proved to be the reason for such energy separation. The observed distance for energy separation was $\sim 50 \text{ nm}$ for flat GNR systems. An energy barrier was observed in the right-angle bent GNR, which was caused mainly by two factors: one is the phonon energy

scattering and reflection at the bending structure, and the other one is that the compressive strain in the bending area that could increase the local phonon scattering and reduce thermal conductivity. The bending resistance (R) for the $2.0 \times 25.0 \text{ nm}^2$ right-angle bent GNR was calculated to be 1.48×10^{-11} and $3.93 \times 10^{-11} \text{ K m}^2 \text{ W}^{-1}$ before and after quantum correction. When the phonon packages passed through the bending structure, instead of keeping the vibrating directions, they preserved their vibrating modes, *i.e.* the ZM phonon branch will always vibrate in the out-of-plane direction, and TM and LM phonon branches will always vibrate perpendicular and parallel to the phonon propagating direction. No obvious bending resistance was observed in the 135° bent GNR structure.

Acknowledgements

Support of this work from the Office of Naval Research (N000141210603) and National Science Foundation (no. CMMI-1029072, CBET-0931290) is gratefully acknowledged.

References

- 1 K. I. Bolotin, K. J. Sikes, Z. Jiang, M. Klima, G. Fudenberg, J. Hone, P. Kim and H. L. Stormer, *Solid State Commun.*, 2008, **146**, 351–355.
- 2 C. Lee, X. D. Wei, J. W. Kysar and J. Hone, *Science*, 2008, **321**, 385–388.
- 3 A. K. Geim and K. S. Novoselov, *Nat. Mater.*, 2007, **6**, 183–191.
- 4 K. S. Novoselov, D. Jiang, F. Schedin, T. J. Booth, V. V. Khotkevich, S. V. Morozov and A. K. Geim, *Proc. Natl. Acad. Sci. U. S. A.*, 2005, **102**, 10451–10453.
- 5 F. Schedin, A. K. Geim, S. V. Morozov, E. W. Hill, P. Blake, M. I. Katsnelson and K. S. Novoselov, *Nat. Mater.*, 2007, **6**, 652–655.
- 6 A. A. Balandin, S. Ghosh, W. Z. Bao, I. Calizo, D. Teweldebrhan, F. Miao and C. N. Lau, *Nano Lett.*, 2008, **8**, 902–907.
- 7 A. A. Balandin, *Nat. Mater.*, 2011, **10**, 569–581.
- 8 S. Ghosh, I. Calizo, D. Teweldebrhan, E. P. Pokatilov, D. L. Nika, A. A. Balandin, W. Bao, F. Miao and C. N. Lau, *Appl. Phys. Lett.*, 2008, **92**, 151911.
- 9 J. U. Lee, D. Yoon, H. Kim, S. W. Lee and H. Cheong, *Phys. Rev. B: Condens. Matter Mater. Phys.*, 2011, **83**, 081419.
- 10 W. W. Cai, A. L. Moore, Y. W. Zhu, X. S. Li, S. S. Chen, L. Shi and R. S. Ruoff, *Nano Lett.*, 2010, **10**, 1645–1651.
- 11 S. S. Chen, A. L. Moore, W. W. Cai, J. W. Suk, J. H. An, C. Mishra, C. Amos, C. W. Magnuson, J. Y. Kang, L. Shi and R. S. Ruoff, *ACS Nano*, 2011, **5**, 321–328.
- 12 J. H. Seol, I. Jo, A. L. Moore, L. Lindsay, Z. H. Aitken, M. T. Pettes, X. S. Li, Z. Yao, R. Huang, D. Broido, N. Mingo, R. S. Ruoff and L. Shi, *Science*, 2010, **328**, 213–216.
- 13 J. N. Hu, X. L. Ruan and Y. P. Chen, *Nano Lett.*, 2009, **9**, 2730–2735.
- 14 W. J. Evans, L. Hu and P. Keblinski, *Appl. Phys. Lett.*, 2010, **96**, 203112.
- 15 H. J. Zhang, G. Lee, A. F. Fonseca, T. L. Borders and K. Cho, *J. Nanomater.*, 2010, **2010**, 537657.

- 16 Z. X. Guo, D. Zhang and X. G. Gong, *Appl. Phys. Lett.*, 2009, **95**, 163103.
- 17 J. C. Zhang, X. P. Huang, Y. N. Yue, J. M. Wang and X. W. Wang, *Phys. Rev. B: Condens. Matter Mater. Phys.*, 2011, **84**, 235416.
- 18 D. L. Nika, E. P. Pokatilov, A. S. Askerov and A. A. Balandin, *Phys. Rev. B: Condens. Matter Mater. Phys.*, 2009, **79**, 155413.
- 19 D. L. Nika, S. Ghosh, E. P. Pokatilov and A. A. Balandin, *Appl. Phys. Lett.*, 2009, **94**, 203103.
- 20 P. G. Klemens, *Int. J. Thermophys.*, 2001, **22**, 265–275.
- 21 P. G. Klemens, *J. Wide Bandgap Mater.*, 2000, **7**, 332–339.
- 22 K. Saito, J. Nakamura and A. Natori, *Phys. Rev. B: Condens. Matter Mater. Phys.*, 2007, **76**, 115409.
- 23 R. Prasher, *Science*, 2010, **328**, 185–186.
- 24 L. Lindsay, D. A. Broido and N. Mingo, *Phys. Rev. B: Condens. Matter Mater. Phys.*, 2010, **82**, 115427.
- 25 L. Lindsay, D. A. Broido and N. Mingo, *Phys. Rev. B: Condens. Matter Mater. Phys.*, 2011, **83**, 235428.
- 26 W. F. Chen and L. F. Yan, *Nanoscale*, 2011, **3**, 3132–3137.
- 27 L. Liao, Y. C. Lin, M. Q. Bao, R. Cheng, J. W. Bai, Y. A. Liu, Y. Q. Qu, K. L. Wang, Y. Huang and X. F. Duan, *Nature*, 2010, **467**, 305–308.
- 28 Y. M. Lin, C. Dimitrakopoulos, K. A. Jenkins, D. B. Farmer, H. Y. Chiu, A. Grill and P. Avouris, *Science*, 2010, **327**, 662.
- 29 X. Huang, X. Y. Qi, F. Boey and H. Zhang, *Chem. Soc. Rev.*, 2012, **41**, 666–686.
- 30 T. Kuilla, S. Bhadra, D. H. Yao, N. H. Kim, S. Bose and J. H. Lee, *Prog. Polym. Sci.*, 2010, **35**, 1350–1375.
- 31 S. Stankovich, D. A. Dikin, G. H. B. Dommett, K. M. Kohlhaas, E. J. Zimney, E. A. Stach, R. D. Piner, S. T. Nguyen and R. S. Ruoff, *Nature*, 2006, **442**, 282–286.
- 32 T. T. Baby and S. Ramaprabhu, *J. Mater. Chem.*, 2011, **21**, 9702–9709.
- 33 V. Eswaraiah, V. Sankaranarayanan and S. Ramaprabhu, *ACS Appl. Mater. Interfaces*, 2011, **3**, 4221–4227.
- 34 W. Yu, H. Q. Xie, X. P. Wang and X. W. Wang, *Phys. Lett. A*, 2011, **375**, 1323–1328.
- 35 D. W. Brenner, O. A. Shenderova, J. A. Harrison, S. J. Stuart, B. Ni and S. B. Sinnott, *J. Phys.: Condens. Matter*, 2002, **14**, 783–802.
- 36 B. W. Dodson, *Phys. Rev. B: Condens. Matter Mater. Phys.*, 1987, **35**, 2795–2798.
- 37 J. Tersoff, *Phys. Rev. Lett.*, 1988, **61**, 2879–2882.
- 38 P. Kim, L. Shi, A. Majumdar and P. L. McEuen, *Phys. Rev. Lett.*, 2001, **87**, 215502.
- 39 J. Hone, M. Whitney, C. Piskoti and A. Zettl, *Phys. Rev. B: Condens. Matter Mater. Phys.*, 1999, **59**, R2514–R2516.
- 40 A. Cao, *J. Appl. Phys.*, 2012, **111**, 083528.
- 41 J. N. Hu, S. Schiffl, A. Vallabhaneni, X. L. Ruan and Y. P. Chen, *Appl. Phys. Lett.*, 2010, **97**, 133107.
- 42 N. Yang, G. Zhang and B. W. Li, *Appl. Phys. Lett.*, 2009, **95**, 033107.
- 43 X. M. Yang, A. C. To and R. Tian, *Nanotechnology*, 2010, **21**, 155704.
- 44 D. K. Efetov and P. Kim, *Phys. Rev. Lett.*, 2010, **105**, 256805.
- 45 F. P. Incropera, D. P. Dewitt, T. L. Bergman and A. S. Lavine, *Fundamentals of Heat and Mass Transfer*, (Sixth Edition), Wiley, Hoboken, NJ, 2007.
- 46 J. N. Hu, X. L. Ruan, Z. G. Jiang and Y. P. Chen, *AIP Conf. Proc.*, 2009, **1173**, 135–138.
- 47 Y. N. Yue, J. C. Zhang and X. W. Wang, *Small*, 2011, **7**, 3324–3333.
- 48 Z. Chen, W. Jang, W. Bao, C. N. Lau and C. Dames, *Appl. Phys. Lett.*, 2009, **95**, 161910.
- 49 M. Chester, *Phys. Rev.*, 1963, **131**, 2013.
- 50 X. Xu and X. Wang, *Appl. Phys. A: Mater. Sci. Process.*, 2001, **73**, 107–114.
- 51 X. B. Li, K. Maute, M. L. Dunn and R. G. Yang, *Phys. Rev. B: Condens. Matter Mater. Phys.*, 2010, **81**, 245318.
- 52 S. Bhowmick and V. B. Shenoy, *J. Chem. Phys.*, 2006, **125**, 164513.
- 53 C. Liang and K. Satish, *J. Appl. Phys.*, 2012, **112**, 043502.